Applied Catalysis B: Environmental 154–155 (2014) 51–61

Contents lists available at ScienceDirect

Applied Catalysis B: Environmental

journal homepage: www.elsevier.com/locate/apcatb

Palladium doped perovskite-based NO oxidation catalysts: The role of Pd and B-sites for NO_x adsorption behavior via in-situ spectroscopy

Zafer Say[a], Merve Dogac[a], Evgeny I. Vovk[a,b], Y. Eren Kalay[c], Chang Hwan Kim[d], Wei Li[d], Emrah Ozensoy[a,*]

[a] Department of Chemistry, Bilkent University, 06800 Ankara, Turkey
[b] Boreskov Institute of Catalysis, 630090 Novosibirsk, Russian Federation
[c] Department of Metallurgical & Materials Engineering, Middle East Technical University, 06800 Ankara, Turkey
[d] General Motors Global R&D Chemical Sciences & Materials Systems Lab, 30500 Mound Rd., Warren, MI 48090, USA

ARTICLE INFO

Article history:
Received 1 November 2013
Received in revised form 13 January 2014
Accepted 20 January 2014
Available online 28 January 2014

Keywords:
$LaCoO_3$
$LaMnO_3$
Pd
NO_x
$DeNO_x$

ABSTRACT

Perovskite-based materials ($LaMnO_3$, $Pd/LaMnO_3$, $LaCoO_3$ and $Pd/LaCoO_3$) were synthesized, characterized (via BET, XRD, Raman spectroscopy, XPS and TEM) and their NO_x ($x = 1,2$) adsorption characteristics were investigated (via in-situ FTIR and TPD) as a function of the nature of the B-site cation (i.e. Mn vs Co), Pd/PdO incorporation and H_2-pretreatment. NO_x adsorption on of $LaMnO_3$ was found to be significantly higher than $LaCoO_3$, in line with the higher SSA of $LaMnO_3$. Incorporation of PdO nanoparticles with an average diameter of ca. 4 nm did not have a significant effect on the amount of NO_2 adsorbed on fresh $LaMnO_3$ and $LaCoO_3$. TPD experiments suggested that saturation of fresh $LaMnO_3$, $Pd/LaMnO_3$, $LaCoO_3$ and $Pd/LaCoO_3$ with NO_2 at 323 K resulted in the desorption of NO_2, NO, N_2O and N_2 (without O_2) below 700 K, while above 700 K, NO_x desorption was predominantly in the form of $NO + O_2$. Perovskite materials were found to be capable of activating N–O linkages typically at ca. 550 K (even in the absence of an external reducing agent) forming N_2 and N_2O as direct NO_x decomposition products. H_2-pretreatment yielded a drastic boost in the NO oxidation and NO_x adsorption of all samples, particularly for the Co-based systems. Presence of Pd further boosted the NO_x uptake upon H_2-pretreatment. Increase in the NO_x adsorption of H_2-pretreated $LaCoO_3$ and $Pd/LaCoO_3$ surfaces could be associated with the electronic changes (i.e. reduction of B-site cation), structural changes (surface reconstruction and SSA increase), reduction of the precious metal oxide (PdO) into metallic species (Pd), and the generation of oxygen defects on the perovskite. Mn-based systems were more resilient toward B-site reduction. Pd-addition suppressed the B-site reduction and preserved the ABO_3 perovskite structure.

1. Introduction

NO_x (i.e. predominantly NO, NO_2) is one of the main pollutants emitted by diesel and gasoline-powered engines and has a significantly negative influence on the environment. During the last two decades, emission regulations have become tighter, and numerous technologies for NO_x after-treatment have been developed and commercialized. For the conventional gasoline engines, three-way catalysts (TWC) can reduce toxic gases effectively under a stoichiometric air to fuel ratio (14.5); however TWC is not effective in NO_x after treatment in diesel engines operating under oxygen-rich lean conditions (where the air to fuel ratio greater than 14.5). NO_x storage reduction (NSR) catalysts were developed as an alternative technology [1–3]. Conventional NSR catalysts are composed of three main components, Pt, Al_2O_3, and BaO where BaO functions as the NO_x storage component. Although the presence of Pt is critical for NO oxidation (an important step in NO_x storage), it contributes significantly to the total cost of the catalyst. These important drawbacks led the direction of research toward noble metal-free materials.

Perovskites in the form of ABO_3 have been considered as promising alternatives for low-cost automotive catalysts with excellent redox properties and high thermal durability [4,5]. The chemical properties of the perovskite materials are also known for their flexible characteristics which are associated with their A and/or B site substitution capabilities and availability of a wide variety of sub-stoichiometric structures [6]. The catalytic efficiencies of perovskite materials for NO and N_2O reduction into N_2 were demonstrated by several studies [7–13]. Moreover, these materials play an efficient role in the catalytic NO oxidation under lean conditions even in the absence of a noble metal [14,15]. Recently, Kim et al. [16] reported that Sr-promoted La-based perovskite catalysts

* Corresponding author. Tel.: +90 3122902121; fax: +90 3122664068.
E-mail address: ozensoy@fen.bilkent.edu.tr (E. Ozensoy).

0926-3373/$ – see front matter © 2014 Elsevier B.V. All rights reserved.
http://dx.doi.org/10.1016/j.apcatb.2014.01.038

($La_{1-x}Sr_xCoO_3$) exhibit higher catalytic NO to NO_2 conversion rates as compared to Pt-based catalysts.

$LaCoO_3$ and $Pd/LaCoO_3$ based perovskite materials are known to be highly sensitive toward pretreatment under reducing conditions leading to significant structural changes and reconstruction [12,17,18] where the reduction of the perovskite lattice is closely linked to the nature of the B-site cation in the ABO_3 structure. In the current work, the effect of H_2(g) pre-treatment on NO_x oxidation and adsorption over $LaCoO_3$, $LaMnO_3$ as well as their Pd-enriched forms were investigated by means of in-situ Fourier transform infrared (FTIR) spectroscopy and temperature programmed desorption (TPD) in an attempt to provide fundamental knowledge associated with the influence of the nature of the B-site cation and the Pd incorporation on the $DeNO_x$ catalytic chemistry of perovskites.

2. Experimental

2.1. Catalyst preparation

$LaCoO_3$ and $LaMnO_3$, were synthesized via citric acid method involving a citrate route as prescribed in a recent GM patent [19]. Supported palladium catalysts were prepared using classical incipient wetness impregnation method utilizing palladium nitrate together with $LaCoO_3$ or $LaMnO_3$. Pd was impregnated onto the synthesized perovskite samples after the calcination of the perovskites at 973 K for 5 h in air. The nominal loading of palladium was adjusted to 1.5 wt% Pd. Pd incorporated materials were subsequently calcined at 773 K for 5 h in air. The La_2O_3 benchmark material was synthesized via direct calcination of a $La(NO_3)_3{\cdot}6H_2O_{(s)}$ (Sigma Aldrich) precursor at 973 K in an open-air oven for 12 h.

Prior to in-situ FTIR analysis, perovskite samples mounted on the spectroscopic batch reactor were initially treated and activated with an exposure of 2 Torr NO_2(g) for 5 min at 323 K followed by annealing and surface cleaning in vacuum ($<10^{-3}$ Torr) at 973 K. Finally, samples were cooled to 323 K for subsequent NO_2(g) adsorption experiments. The perovskite materials referred in the text as *pre-reduced* were treated with 5.0 Torr H_2(g) (Linde GmbH, Germany, >99.9) at 623 K for 10 min.

NO_2 saturation of the synthesized materials was carried out typically by dosing 5.0 Torr NO_2(g) over the sample for 10 min at 323 K. NO_2(g) used in the experiments was prepared by mixing NO(g) (Air Products, 99.9%) and O_2(g) (Linde GmbH, Germany, 99.999%) followed by multiple freeze-pump-thaw cycles for further purification.

2.2. Instrumentation

All of the FTIR spectroscopic experiments were conducted in transmission mode using a Bruker Tensor 27 spectrometer coupled to a batch-type catalytic reactor whose details have been described elsewhere [20,21]. All of the FTIR spectra were collected at 323 K. All of the adsorption/pre-treatment steps were also performed in batch mode.

Prior to TPD experiments, sample were mounted on the spectroscopic batch reactor and then were exposed to 5.0 Torr NO_2(g) for 10 min. TPD experiments were carried out in vacuum, with a heating rate of 12 K/min. For TPD experiments a quadrupole mass spectrometer (QMS, Stanford Research Systems, RGA 200) was used. The QMS signals with m/z equal to 18 (H_2O), 28 (N_2/CO), 30 (NO/NO_2), 32 (O_2), 44 (N_2O/CO_2), and 46 (NO_2) were monitored during the TPD measurements. It is well known that due to the hard ionization process in the QMS, pure NO_2(g) undergoes fragmentation yielding two major components namely, NO (m/z = 30) and NO_2 (m/z = 46). The NO:NO_2 ratio in the NO_2 fragmentation pattern varies between 3.0 and 4.0 as a function of the ionization conditions. Under the current experimental conditions, fragmentation ratio of NO:NO_2 was determined to be 3.23. In the current work, a strictly quantitate analysis of the TPD desorption channels will not be given. However, using the fragmentation characteristics of pure NO_2(g), relative contributions of pure NO(g) and pure NO_2(g) to the overall m/z = 30 signal can be readily distinguished.

Ex-situ XPS analysis was performed using a SPECS XPS spectrometer with a PHOIBOS-100 hemispherical energy analyzer and a DLD detector utilizing monochromatic Al$K\alpha$ X-ray irradiation ($h\nu$ = 1486.7 eV, 400 W). Instrumental details regarding the other utilized experimental techniques (i.e. XRD, TEM, BET, TPD and Raman spectroscopy) were described elsewhere [20,22].

3. Results and discussion

3.1. Characterization of the synthesized samples via XRD, TEM, BET, XPS, and Raman spectroscopy

Fig. 1 illustrates the ex-situ XRD profiles of $LaMnO_3$, $Pd/LaMnO_3$, $LaCoO_3$ and $Pd/LaCoO_3$ materials obtained after synthesis and calcination at 973 K. XRD patterns verify that synthesis of perovskite structures was achieved as indicated by the presence of the characteristic diffraction lines at 32.56° ($LaMnO_3$) as well as 32.84° and 33.21° ($LaCoO_3$) [23]. This major diffraction signal possesses additional information about the lattice structure of perovskite materials as shown in detail in Fig. 1b. While Mn-based perovskite structures have only a single major peak related to the cubic lattice or poorly crystalline rhombohedral structure, Co-based perovskites reveal a doublet indicating a transformation from cubic into rhombohedral structure [24]. Another critical feature presented in Fig. 1b is the shift in 2-theta value from 32.56° to 32.84°. This can be explained by the smaller lattice spacing of Co-based materials due to smaller ionic size of Co^{3+}. XRD data given in Fig. 1 point out that after Pd impregnation, the only detectable phases were perovskite phases and no other ordered phases such as La_2O_3, MnO_x, CoO_x, Pd or PdO were visible. Lack of such signals is likely due to the small particle size, low volume percentile or lack of crystallographic order in such phases. As illustrated in the TEM images of Pd-impregnated materials given in Fig. 2, PdO/PdO_x particles are clearly visible and are dispersed on the perovskite surface with an average particle size of ca. 4 nm. It is worth mentioning that PdO/PdO_x nanoparticles on the synthesized nanoparticles have a relatively low surface mobility which enables a relatively good PdO/PdO_x dispersion even after calcination at 773 K. Assuming atomic dispersion for PdO_x particles and a $LaMnO_3$ surface atom density of 10^{15} atoms/cm^2, a simple estimation reveals that surface dispersion of PdO_x is ca. 38%. However, TEM images in Fig. 2 suggest that average PdO_x particle size is ~4 nm indicating that the actual PdO_x dispersion is smaller than the estimated value. The oxidic character of the Pd particles (i.e. the presence of Pd^{x+}/Pd^{2+} species) is evident by a ca. +1.5 eV shift in the Pd3d XPS binding energy (B.E.) values observed for the $Pd/LaMnO_3$ and $Pd/LaCoO_3$ samples (see the Supporting information section) compared to the typical metallic Pd3d B.E. of 335.3 eV.

The results of the BET specific surface area (SSA) measurements of the synthesized samples are presented in Fig. 3. The Mn-based samples calcined at 973 K have comparatively higher SSAs which are approximately 20 m^2/g. On the other hand, SSAs of Co-based samples are ca. 8 m^2/g. Temperature-dependent structural evolution by means of XRD analysis (data not shown) of perovskite materials reveals that structural transformation from amorphous to a crystalline structure takes place at a relatively lower temperature for $LaCoO_3$. While $LaCoO_3$ has a cubic crystalline structure at 873 K, $LaMnO_3$ is still amorphous at the same temperature.

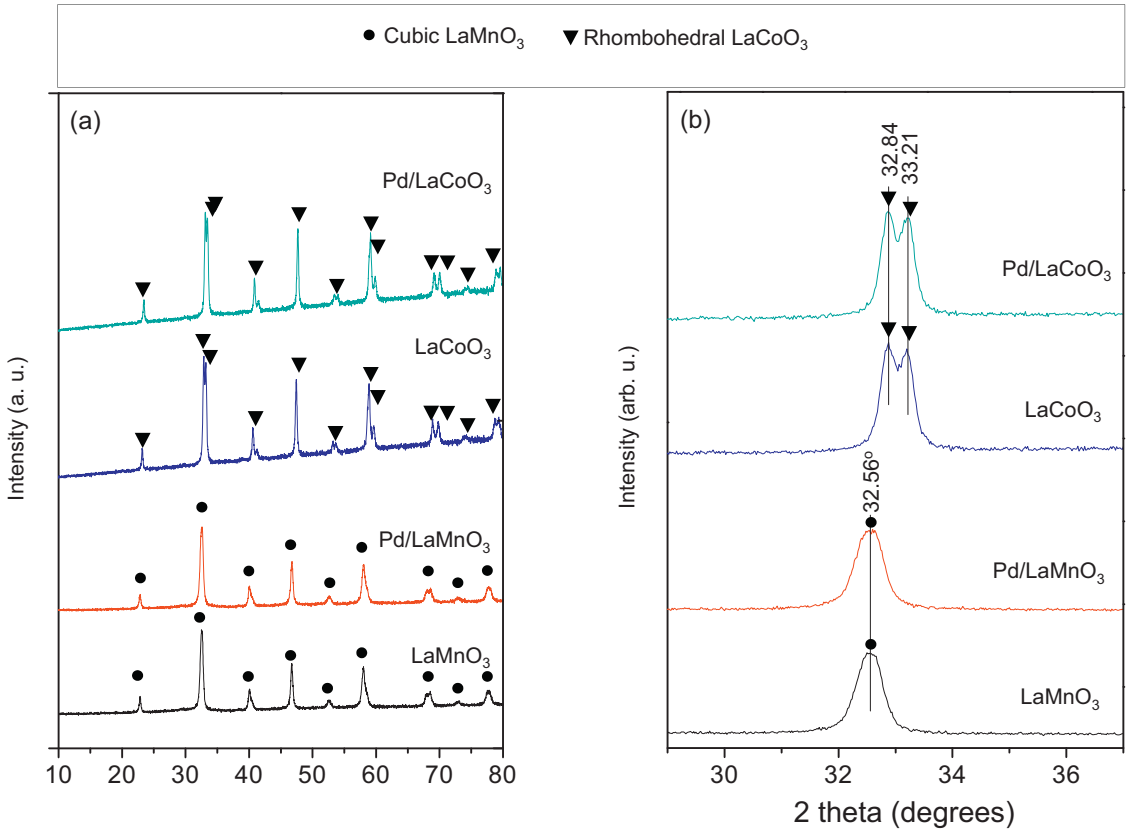

Fig. 1. (a) Ex-situ XRD patterns corresponding to $LaMnO_3$, $Pd/LaMnO_3$, $LaCoO_3$ and $Pd/LaCoO_3$ samples after calcination at 973 K for 5 h. (b) Detailed XRD pattern between $29^\circ < 2\theta < 37^\circ$.

Therefore, it is apparent that Mn-based perovskites reveal higher SSA values and are less ordered than their Co-based counterparts. Interestingly, Co-based catalyst was reported to be significantly more active than Mn-based catalyst [16] suggesting that the intrinsic rate of NO oxidation over $LaCoO_3$ catalyst could be much greater than that of $LaMnO_3$. Moreover, Fig. 3 illustrates that Pd addition causes only a minor increase in the SSA (i.e. ~1–2 m^2/g) for both Mn- and Co-based perovskites.

Raman spectroscopy could be a useful technique in order to identify various phases in the material structure which might be elusive to detect in XRD due to poor crystallinity or small particle size. Thus, Raman spectroscopic characterization of the synthesized materials has also been performed in order to check the presence of additional phases other than the perovskite phases. Raman spectra of $LaMnO_3$, $Pd/LaMnO_3$, $LaCoO_3$ and $Pd/LaCoO_3$ are presented in Fig. 4. $LaMnO_3$ and $Pd/LaMnO_3$ samples reveal three major Raman features at ca. 205, 421 and 644 cm^{-1} as illustrated in Fig. 4a and b, respectively. The former features at 210 and 421 cm^{-1} can be associated with A_{1g} and E_g modes of oxygen cage rotation and vibration in $LaMnO_3$ perovskite, respectively [25]. Another Raman feature at 644 cm^{-1} can be attributed to a Mn–O–Mn stretching mode ($\nu_{Mn-O-Mn}$) in the perovskite structure in accordance with Li et al. [26] who reported a similar peak at 654 cm^{-1} for Mn_3O_4, as well as Ammundsen et al. [27] who also reported a Raman signal at 647 cm^{-1} for MnO_2. Furthermore, this assignment is also consistent with the previously published Raman data on $Pd/LaMnO_3$ [28] which revealed a major signal at 653 cm^{-1}. There is also another weak feature located at ca. 520 cm^{-1} corresponding to the $LaMnO_3$ and $Pd/LaMnO_3$ samples. Xi et al. reported that this weak feature might be related to fluorescence bands [29]. Moreover, Iliev et al. assigned this weak feature to the A_g Raman active mode of the perovskite structure [30].

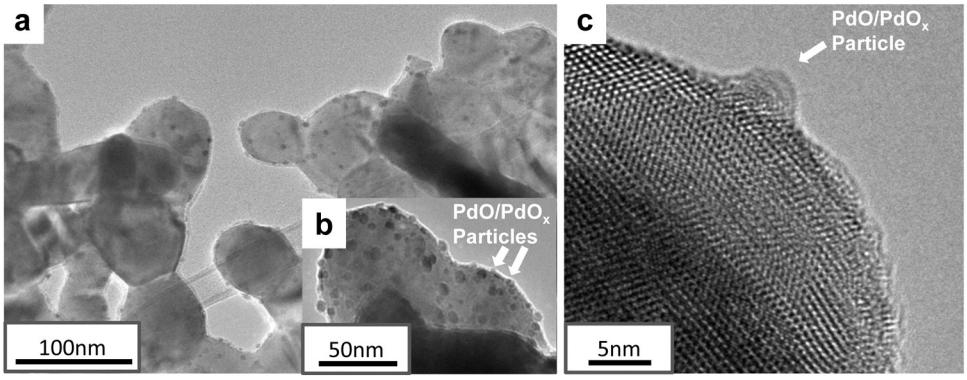

Fig. 2. Representative TEM images for ((a) and (b)) $Pd/LaMnO_3$ and (c) $Pd/LaCoO_3$ that were initially calcined at 973 K for 5 h.

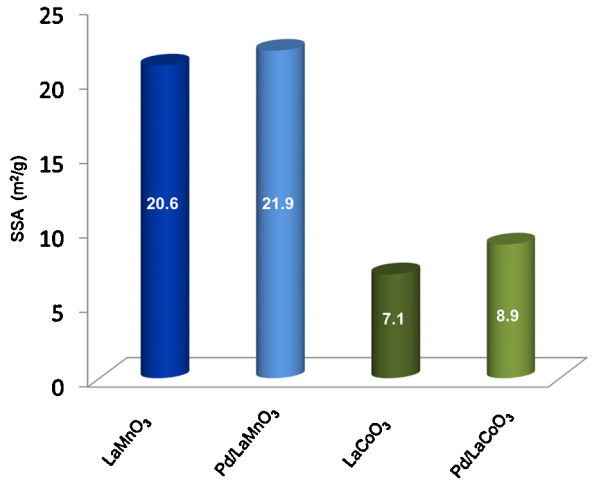

Fig. 3. BET specific surface area values for $LaMnO_3$, $Pd/LaMnO_3$, $LaCoO_3$ and $Pd/LaCoO_3$ after calcination at 973 K for 5 h.

As shown in Fig. 4 spectra (c) and (d), $LaCoO_3$ and $Pd/LaCoO_3$ materials exhibit a Raman scattering feature at ca. 409 cm^{-1} and a weak broad feature at ca. 612 cm^{-1}. The 409 cm^{-1} feature can be associated with the perovskite structure. Tang et al. investigated the Raman spectra of different cobalt containing compounds such as CoOOH, Co_3O_4 and CoO; and observed a sharp feature at ca. 650 cm^{-1} [31]. Thus, it is likely that the feature at 615 cm^{-1} in spectra (c) and (d) is associated with Co–O species.

Fig. 5 illustrates the relative surface atomic ratios of the synthesized materials obtained via XPS measurements. The atomic ratios were calculated from the corresponding Pd3d, La3d, Mn2p, and Co3p spectra by taking the corresponding XP sensitivity factors into account. For both Pd-free and Pd-containing perovskites, XPS data reveal that the sample surfaces are enriched by La (i.e. Mn/La and Co/La surface atomic ratios are less than 1). La accumulation on the surface most probably occurs due to formation of $La_2(CO_3)_3$, $La(OH)_3$ and/or amorphous La_2O_3 domains together

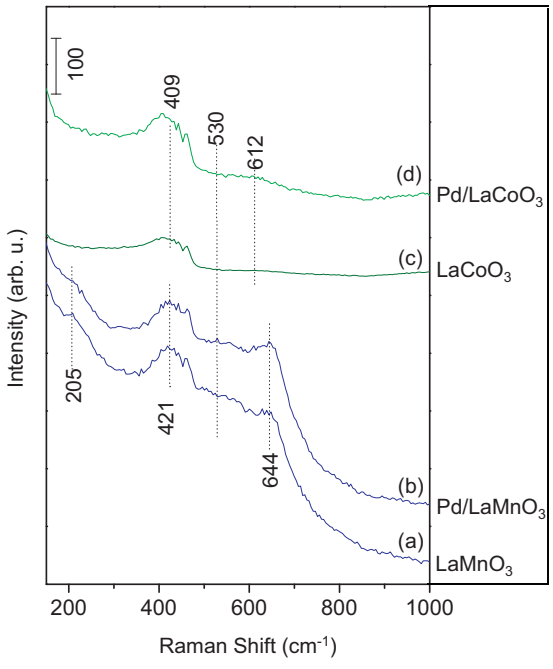

Fig. 4. Ex-situ Raman spectra corresponding to (a) $LaMnO_3$, (b) $Pd/LaMnO_3$, (c) $LaCoO_3$ and (d) $Pd/LaCoO_3$ samples after calcination at 973 K for 5 h.

with the perovskite. As illustrated in a recent study [32], it is possible to control the Co/La surface atomic ratio, by modifying the synthesis parameters. However, the currently used synthesis parameters were chosen in order to mimic the synthetic conditions reported in a recent study by GM [16] which demonstrated highly active perovskite catalysts. The presence of surface carbonate and hydroxide groups is confirmed by the C1s and O1s XP spectra (data not shown). La enrichment of the surfaces can also be associated with a La-terminated perovskite structure which is consistent with recent Density Functional Theory (DFT) calculations of Schneider et al., on the $LaCoO_3$ surface, who reported that the La surface termination is energetically the most favorable termination for the $LaCoO_3$ unit cell [33]. It is worth mentioning that Pd loading does not affect the Mn/La and Co/La surface atomic ratios.

3.2. NO_2 adsorption/desorption behavior of perovskite surfaces

Fig. 6 presents the FTIR spectra obtained for the stepwise NO_2(g) adsorption on $LaMnO_3$ (Fig. 6a), $LaCoO_3$ (Fig. 6b) and La_2O_3 (Fig. 6c) samples at 323 K. FTIR spectra yield a convoluted set of bands corresponding to various types of nitrates and nitrites with different surface adsorption geometries [34–40]. Vibrational features appearing at 1649 and 1009 cm^{-1} are assigned to asymmetric and symmetric stretching modes of bridging nitrate species on the perovskite surface, respectively [34]. It is evident that bridging nitrates are readily visible on the $LaMnO_3$ perovskite, while these species are less pronounced on the $LaCoO_3$ surface. Another type of adsorbed nitrate, revealing vibrational features at 1530 and 1269 cm^{-1} can be assigned to monodentate nitrates [37]. Two characteristic vibrational modes of bidentate nitrates are also observed on the surface which are located at 1568 and 1246 cm^{-1} [35,36]. The vibrational bands at 1434, 1322 and 804 cm^{-1} in Fig. 6a (and similar bands in Fig. 6b) can be assigned to $\nu_{N=O}$, ν_{N-O} and δ_{ONO} vibrations of monodentate surface nitrites (–O–N=O), respectively [37–40]. The weak absorption bands at 1090 and 1194 cm^{-1} which are apparent only at the initial stage of NO_2(g) exposure and disappear at higher exposures can be assigned to bridging and/or chelating nitrites [11]. The simultaneous growth of nitrate and nitrite species can be associated with the disproportionation of NO_2 on the perovskites surfaces:

$$2NO_2(ads) + O^{2-}(surf) \rightarrow NO_3^-(ads) + NO_2^-(ads)$$

Fig. 6 suggests that during the initial stages of NO_2 adsorption, bridging nitrates and bridging/chelating nitrites are formed. With further NO_2 exposure, the bridging/chelating nitrite are transformed into surface nitrito species while bridging nitrate signals continue to grow together with monodentate and bidentate nitrates. Further NO_2 exposure leads to the simultaneous growth of the nitrates and monodentate nitrite (nitrito) species until the surfaces are saturated with NO_x. Along these lines, it is apparent that on the investigated perovskite surfaces, NO_2 adsorption is predominantly accompanied with its oxidation to nitrate species. Thus, the surface coverage of nitrates on the investigated perovskites not only reveals the relative amount of NO_x adsorption but it can also be an indirect indicator associated with the inherent NO oxidation capabilities of these surfaces.

It is visible that the general aspects of the vibrational spectra corresponding to NO_x adsorption geometries of two different perovskite surfaces show significant resemblances. This behavior can be explained by considering the XPS results given in Fig. 5, which clearly show that both $LaMnO_3$ and $LaCoO_3$ surfaces are La-enriched. As discussed earlier, this can either be attributed to La-terminated perovskite surfaces or the presence of additional amorphous La_2O_3 (and/or $La_2(CO_3)_3$, $La(OH)_3$) domains on both surfaces revealing similar adsorbed NO_x species for $LaMnO_3$ and

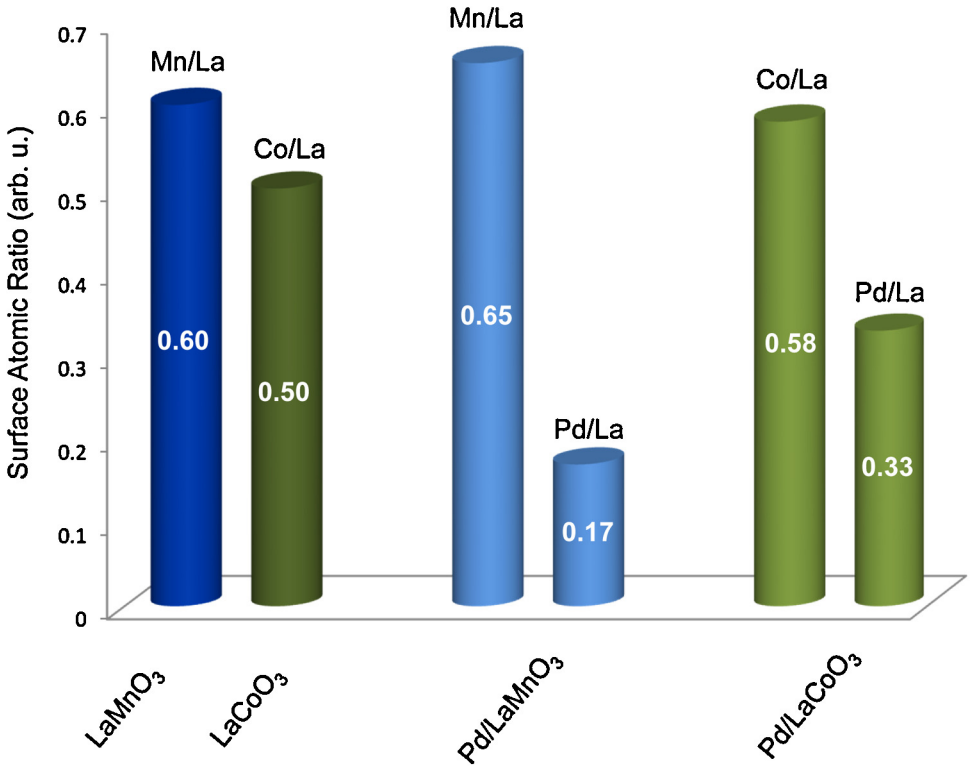

Fig. 5. Quantitative determination of the surface atomic ratios via XPS for the synthesized $LaMnO_3$, $Pd/LaMnO_3$, $LaCoO_3$ and $Pd/LaCoO_3$ samples after calcination at 973 K for 5 h.

$LaCoO_3$. In other words, on both $LaMnO_3$ and $LaCoO_3$, adsorbed NO_x species are mostly in the form of nitrates which are coordinated to either amorphous La_2O_3 and/or $La_2(CO_3)_3$, $La(OH)_3$ domains or La-terminated perovskite surfaces. In order to have a better insight into surface functional groups, benchmark NO_x adsorption experiments were also performed on pure La_2O_3 as shown in Fig. 6c which reveals similar vibrational frequencies to that of $LaMnO_3$ and $LaCoO_3$. This may suggest that although B-sites may play a crucial role during the initial stages of NO_x adsorption, final adsorption sites of the stored NO_x species on $LaMnO_3$ and $LaCoO_3$ surfaces are more sensitive to the A-sites of the ABO_3 structure, rather than the B-sites.

Another important observation regarding the FTIR data given in Fig. 6 which is worth emphasizing is that total IR signal intensities related to adsorbed NO_x species are quite dissimilar for Co- and Mn-based materials. Assessment of the IR absorbance values for the NO_2-saturated $LaMnO_3$ and $LaCoO_3$ surfaces (i.e. red spectra in Fig. 6a and b), immediately reveals that $LaMnO_3$ adsorbs significantly higher amount of NO_x than $LaCoO_3$, in accordance with its considerably higher specific surface area (Fig. 5).

NO_2 uptake behaviors of Pd-containing and Pd-free perovskite materials were also investigated in a comparative fashion by means of FTIR spectroscopy. Fig. 7 shows the corresponding FTIR spectra obtained after the saturation of $LaMnO_3$, $Pd/LaMnO_3$, $LaCoO_3$ and $Pd/LaCoO_3$ surfaces with 5 Torr NO_2(g) for 10 min at 323 K. It is clearly visible in Fig. 7 that incorporation of Pd species does not significantly alter the nature of the adsorbed NO_x species on both of the perovskite surfaces. In addition, the presence of Pd species result in a minor increase in the IR absorption intensities for both Mn- and Co-based materials which is in good agreement with the slight increase in the specific surface area values of these surfaces as shown in Fig. 5.

Further insight regarding the relationship between NO oxidation and NO_x adsorption as well as the desorption/decomposition

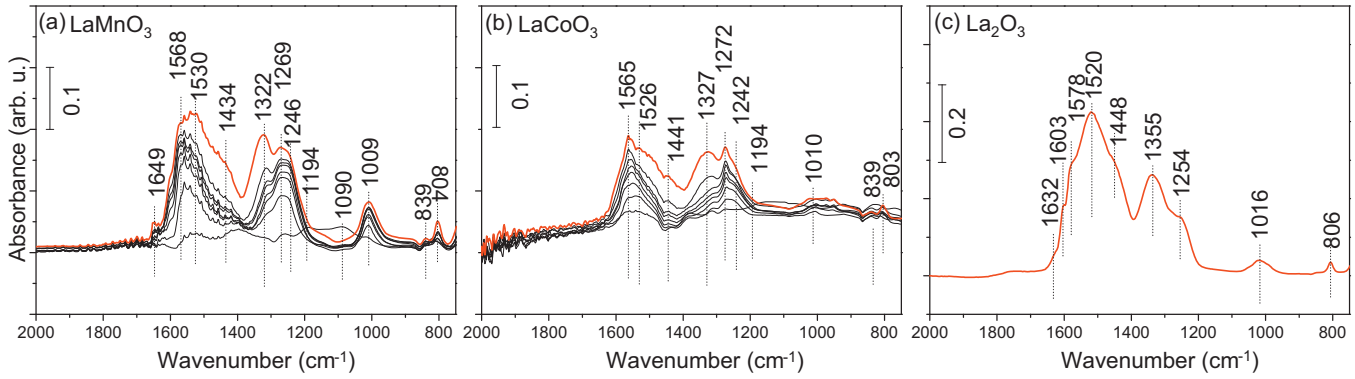

Fig. 6. FTIR spectra corresponding to the stepwise NO_2 adsorption at 323 K on the (a) $LaMnO_3$ (b) $LaCoO_3$ and (c) La_2O_3 samples. The spectra corresponding to the NO_2-saturated (via 5.0 Torr NO_2(g) over the sample surface for 10 min at 323 K) sample surfaces are marked with red spectra.

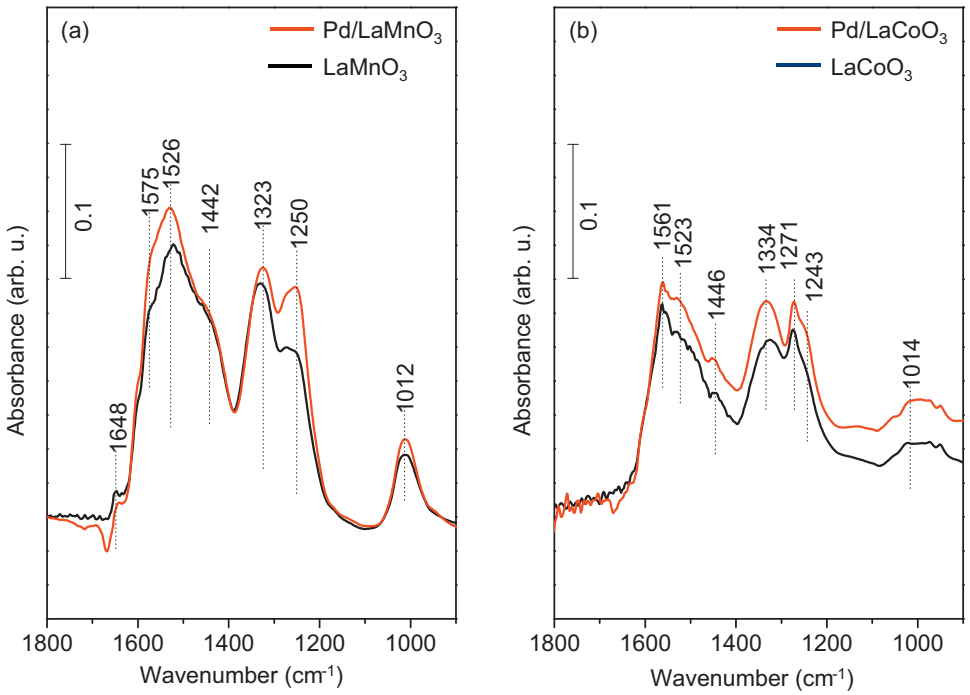

Fig. 7. FTIR spectra corresponding to the NO_2-saturated (a) $LaMnO_3$ and $Pd/LaMnO_3$ and (b) $LaCoO_3$ and $Pd/LaCoO_3$ at 323 K. Black spectra in each panel represent the Pd-free materials and red spectra correspond to Pd-containing materials.

pathways of the adsorbed NO_x species can be obtained via TPD. Fig. 8 illustrates the TPD profiles for $LaMnO_3$, $Pd/LaMnO_3$, $LaCoO_3$ and $Pd/LaCoO_3$ samples obtained after saturation of these surfaces with NO_2 at 323 K (5.0 Torr NO_2 exposure for 10 min) where some of the major desorption channels (m/z = 28, 30, 32, 44, 46 corresponding to N_2, NO, O_2, N_2O and NO_2, respectively) are shown. With the help of the TPD data, NO_x adsorption on $LaMnO_3$ and $LaCoO_3$ can be compared. Such a comparison clearly indicates that $LaMnO_3$ adsorbs a greater amount of NO_x than $LaCoO_3$ in excellent agreement with the current BET (Fig. 3) and in-situ FTIR (Fig. 6)

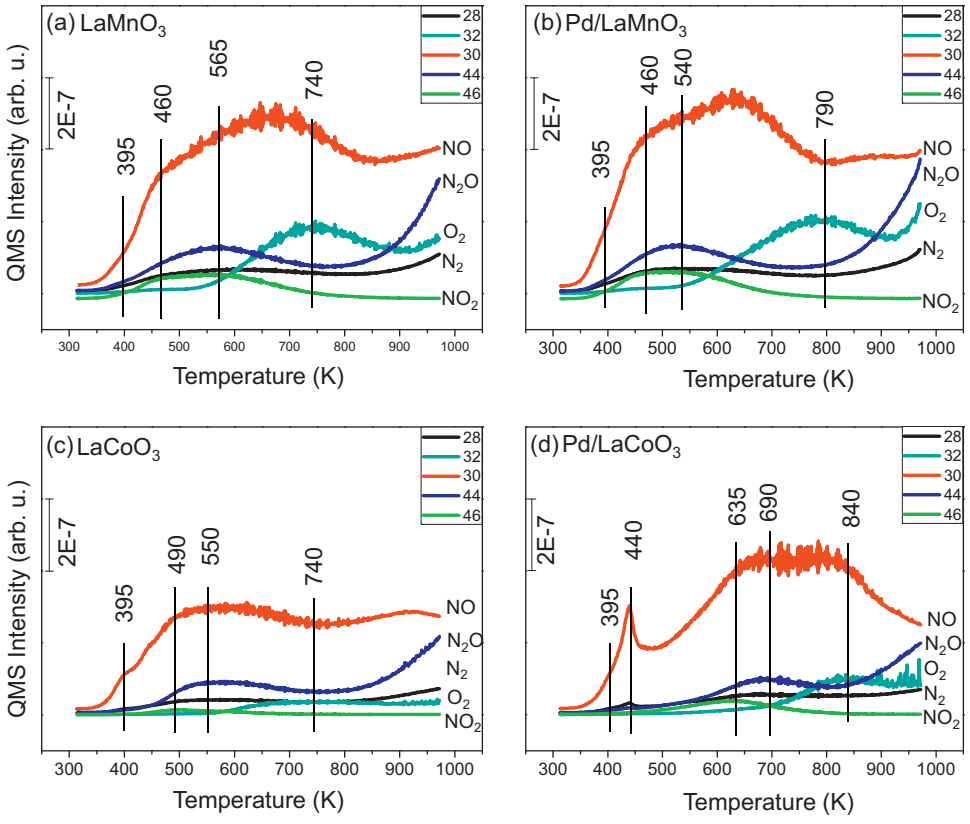

Fig. 8. TPD profiles obtained from (a) $LaMnO_3$, (b) $Pd/LaMnO_3$, (c) $LaCoO_3$ and (d) $Pd/LaCoO_3$ samples after saturation with 5 Torr NO_2(g) at 323 K for 10 min.

measurements. Moreover, integrated $NO + NO_2 + N_2 + N_2O$ TPD signals of $LaMnO_3$ was found to be 48% higher than that of $LaCoO_3$ (see the Supporting information section for details). A detailed analysis of the desorbing species observed in the TPD data given in Fig. 8 suggests that NO desorption occurs in a broad temperature window (i.e. 400–800 K) yielding multiple and convoluted desorption features and a global desorption maximum at ca. 650 K. These convoluted NO desorption features can be better interpreted by analyzing the simultaneously recorded additional desorption channels.

NO_2 ($m/z = 46$) desorption profiles given in Fig. 8a and b corresponding to $LaMnO_3$ and $Pd/LaMnO_3$ samples possess a line shape where at least two desorption states are discernible at ca. 460 and 565 K. It is well-known that pure NO_2(g) can be readily fragmented inside a QMS due to electron impact ionization yielding NO and NO_2 as the major signals, where NO:NO_2 ratio is found to be typically between 3:1 and 4:1. Thus, the characteristic NO desorption features in Fig. 8a and b appearing at 460 and 565 K can be attributed predominantly to NO_2 desorption from the $LaMnO_3$ and $Pd/LaMnO_3$ surfaces with some contribution from NO desorption. It is important to note that these desorption states do not reveal any simultaneous O_2(g) desorption signal. Temperature-programmed FTIR experiments (Supporting information Fig. 1) performed in a parallel fashion to the current TPD experiments indicate that nitrates and nitrito species disappear in a gradual and a simultaneous manner during the heating ramp without a significant change in the line shape of the FTIR spectra. Thus, for the desorption window within 460–570 K, it can be argued that on the $LaMnO_3$ and $Pd/LaMnO_3$ surfaces, nitrito and nitrate species desorb/decompose in the form of NO_2 + NO (without O_2) where the O species generated during nitrate decomposition is captured by the perovskite curing oxygen defects or in the case of $Pd/LaMnO_3$, possibly oxidizing Pd/PdO_x sites into PdO.

Another clearly visible signal appearing simultaneously with the NO and NO_2 desorption channels in the range of 490–570 K in Fig. 8a and b is N_2O ($m/z = 44$). N_2O desorption channel has a desorption maximum at ca. 565 K which is coinciding with the high-temperature NO_2 desorption signal. Detection of N_2O is quite noteworthy as it indicates that even in the absence of an external reducing agent, $LaMnO_3$ and $Pd/LaMnO_3$ surfaces can directly activate N–O linkages in a rather efficient manner and partially reduce nitrate (NO_3^-) and nitrite (NO_2^-) species above 500 K. As the N_2O formation implies the presence of atomic N species generated on the catalyst surface, recombinative desorption of atomic N in the form of N_2 as the direct total reduction product is also likely. As a matter of fact, $m/z = 28$ desorption channel in Fig. 8a and b clearly reveals the presence of N_2 desorption in a very broad temperature window with a local maximum at ca. 565 K. Observation of N_2O and N_2 in the NO_2 TPD of $LaMnO_3$ and $Pd/LaMnO_3$ clearly shows that these surfaces can be promising materials as $DeNO_x$ catalysts, as they can directly reduce stored NO_x species (i.e. nitrates and nitrites) even in the absence of an external reducing agent.

At higher temperatures, an additional TPD feature in the $m/z = 32$ channel becomes apparent in Fig. 8a and b. This strong O_2 desorption signal located within 750–800 K is detected together with an intense NO desorption signal appearing at the same temperature. In other words, in this temperature interval, NO_x species remaining on the surface decompose as $NO + O_2$ with a less significant contribution from N_2 and N_2O (note that NO_2 desorption is not detected at this temperature). Temperature-programmed FTIR studies (Supporting information Fig. 2) suggest that at this temperature nitrito species are the prominently existing NO_x species on $LaMnO_3$ and $Pd/LaMnO_3$ with a smaller contribution from nitrates. Thus, it is apparent that these thermally stable bridging nitrites decompose mostly in the form of $NO + O_2$. It is worth mentioning that the high temperature O_2 desorption feature appearing within 750–800 K can also be associated to the direct oxygen evolution from $LaMnO_3$ and $Pd/LaMnO_3$ and the formation of oxygen vacancies in the perovskite structure or due to the decomposition of PdO [41,42]. As a final note on Fig. 8a and b, it is worth mentioning that the total NO_x adsorption is not significantly altered upon Pd addition to the Mn-based perovskite system where presence of Pd increases the integrated total NO_x ($NO + NO_2 + N_2 + N_2O$) desorption signal by only about 11% (Fig. 9). For the detailed calculation of the integrated total NO_x TPD signals, reader is referred to the Supporting information section.

General desorption characteristics observed for the NO_2 TPD experiments performed on $LaMnO_3$ and $Pd/LaMnO_3$ surfaces are translated to a large extent on the $LaCoO_3$ and $Pd/LaCoO_3$ samples as well (Fig. 8c and d). As discussed earlier, total integrated NO_x desorption signal is about 48% smaller for the $LaCoO_3$ with respect to that of $LaMnO_3$ (Fig. 9). On the other hand, Pd-incorporation seems to have a larger positive influence on the NO_x adsorption for the Co-based systems where the integrated total NO_x ($NO + NO_2 + N_2 + N_2O$) desorption signal increases by about 16% (Fig. 9). Furthermore, Pd addition also increases the thermal stability of the stored NO_x species shifting their desorption signals to higher temperatures. In particular, Fig. 8d also illustrates that Pd addition leads to a sharp low-temperature NO desorption signal located at 400 K. Corresponding temperature-dependent FTIR data indicate that, at these temperatures monodentate and bridging nitrates are partially destroyed. It is also worth emphasizing that this enhanced low-temperature NO desorption signal is concomitant to N_2O and N_2 signals appearing at the same temperature. Thus, it is clear that Pd incorporation has a minor but detectable positive influence on the low-temperature direct total/partial NO_x reduction on the Co-based perovskite systems. This is consistent with the fact that unlike Rh-based catalysts, it is well known that Pd-based catalysts are not very active in direct NO dissociation.

Combination of XPS and TPD data reveals an interesting correlation between the B-site cation/La^{3+} ratio (i.e. the relative number of B-site cations and La^{3+} cations) in the perovskite structure and the corresponding NO_x adsorption quantities. XPS data (Fig. 5) suggests that incorporation Pd into Co-based perovskite structure causes an increase in Co/La atomic ratio by 16% which is followed by a similar relative increase (i.e. 16%) in the total NO_x adsorption (Fig. 9). In a similar fashion, Pd addition to the Mn-based perovskite structure leads to an increase in Mn/La ratio by 8%, which leads to 11% increase in total NO_x adsorption. These trends suggest that B-site cations play a crucial role in the initial NO_2 adsorption and oxidation in the form of nitrates and nitrites. It is feasible that the initial adsorption and oxidation of NO_2 is governed by B-site cations while upon formation of nitrates/nitrites, these NO_x species spill over on the surface La–O sites.

3.3. *Effect of reductive pre-treatment on NO_x uptake and catalyst structure*

Structural integrity and durability are some of the most critical characteristics of a long lasting catalytic system. Preservation of the structural and functional properties of perovskites is rather challenging due to the stoichiometric flexibility of these systems allowing a vast number of compositional variations originating from the alterations in the oxygen defect density and the changes in the oxidation states of B-site cations in the ABO_3 structure. Since many catalytic processes include sequential oxidation and reduction cycles, we have also investigated the NO_x adsorption behavior of the currently synthesized $LaMnO_3$, $Pd/LaMnO_3$, $LaCoO_3$ and $Pd/LaCoO_3$ samples upon their exposure to reducing conditions. It is known that treatment of Co and Mn-based perovskites with an aggressive reducing agent such as H_2(g) at high enough temperatures may cause reversible or irreversible structural changes [6,43]. This was found to be particularly valid for $LaCoO_3$, where

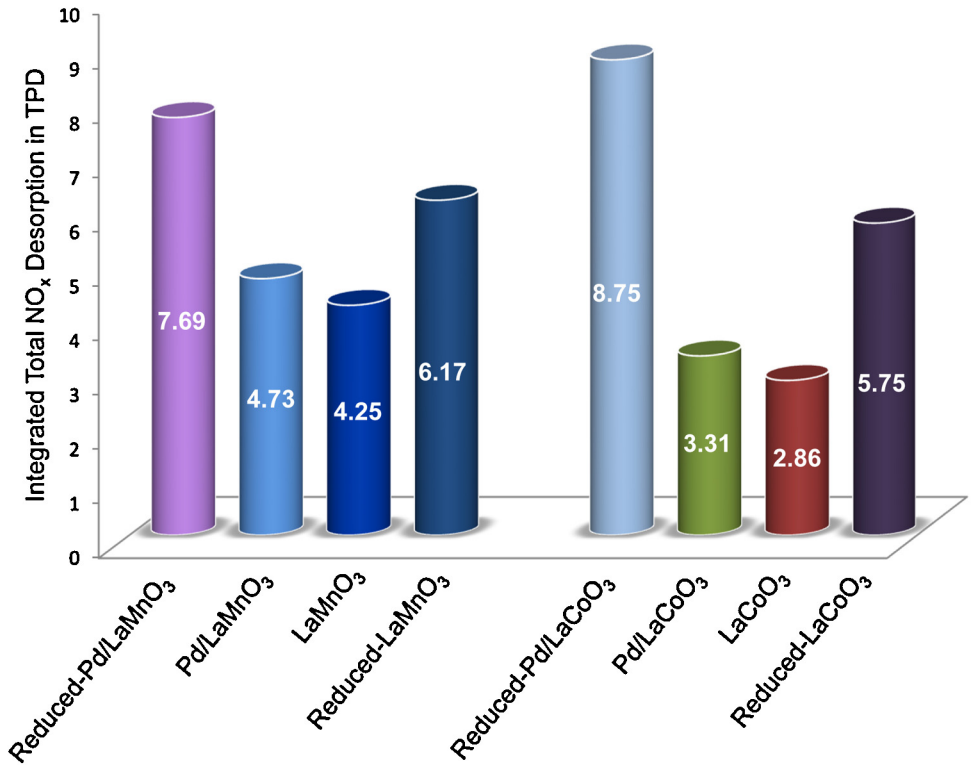

Fig. 9. Integrated total NO_x TPD desorption signals obtained for various NO_2-saturated perovskite materials (see text for details).

Dacquin and Dujardin showed that destruction of the perovskite structure due to the two-step reduction of the B-site cation (via $Co^{3+} \rightarrow Co^{+2} \rightarrow Co^0$) led to the formation of metallic Co and La_2O_3 [44–46].

Thus, in the current study, we have also investigated the NO_x uptake and release properties of $LaMnO_3$, $Pd/LaMnO_3$, $LaCoO_3$ and $Pd/LaCoO_3$ surfaces after pretreating them with H_2. It should be noted that pre-reduction was performed with 5.0 Torr H_2(g) at 623 K for 10 min in batch mode consistent with similar former studies in the literature [46]. Fig. 10 presents such experiments where fresh (red spectra) and H_2 pre-reduced (black spectra) perovskite surfaces were saturated with 5.0 Torr NO_2(g) for 10 min at 323 K.

Fig. 10 illustrates that on the pre-reduced surfaces, abundance of nitrite/nitrito species increases as evident from the relative strengthening of the vibrational frequencies at 1487, ~1450 and 1330 cm^{-1} while nitrate-related vibrational features (e.g. 1567 and 1270 cm^{-1}) attenuate in a relative fashion [35,36].

More importantly, it is visible in Fig. 10 that H_2-pretreatment leads to a drastic increase in the NO_x uptake of both Mn- and Co-based perovskites. Black spectrum in Fig. 10c shows that the radical increase in the NO_x adsorption on the $LaCoO_3$ surface upon H_2 pretreatment is accompanied by a characteristic change in the spectral baseline in the FTIR data which may be associated with an alteration in the electronic structure of the sample. These observations can be explained by the reduction of the $LaCoO_3$ sample and the formation of $Co^0/CoO/La_2O_3$ phases [17]. Implications of such structural alterations are also evident by the formation of two additional spectral features located at 1897 and 1818 cm^{-1} corresponding to dinitrosyl species on Co^{+2} [47–49] (Fig. 10c, black spectrum). Furthermore, it can be seen that Pd-incorporation both enhances the NO_x oxidation (thereby facilitating NO_x adsorption) after H_2-pretreatment (Fig. 10d, black spectrum) and hinders the complete B-site reduction by preserving the structural integrity of the perovskite lattice to a certain extent, evident by a smaller change in the IR spectral baseline (for instance, compare Fig. 10c, black spectrum with Fig. 10d, black spectrum). Influence of the Pd sites on the NO_x adsorption after H_2 treatment can be associated with multiple reasons. For instance, Pd sites in the $Pd/LaCoO_3$ system can facilitate H_2 activation and lead to the formation of reactive CoO_x surface species which can present high activity toward NO oxidation and NO_x uptake without forming a fully reduced form of Co (i.e. Co^0). Alternatively, metallic Pd sites (i.e. Pd^0) created after reduction with H_2 can also directly function as active redox sites providing additional sites for NO_x adsorption.

It is interesting to note that although H_2-pretreatment also boosts the NO_x uptake for the $LaMnO_3$ surface (Fig. 10a, black spectrum) to a certain extent, it is not accompanied by a severe baseline change in the FTIR spectra suggesting the lack of a drastic electronic structural modification. Further support for this argument will be also provided together with the corresponding NO_2 TPD data for the H_2-pretreated surfaces (Fig. 11). In other words, Mn-based samples seem less prone to B-site reduction and the boost in the NO_x adsorption upon H_2-pretreatment and/or Pd addition is less prominent in Mn-based systems. Yet, indications of B-site reduction still exists as seen from the presence of the 1773 cm^{-1} given in the insets of Fig. 10a and b (black spectra), corresponding to nitrosyl species coordinated to Mn^{2+} sites which are generated upon reduction [50].

It is worth mentioning that the ex-situ XPS and XRD measurements obtained immediately after the H_2-pretreatment did not reveal any indications of the presence of reduced La, Co or Mn species. Thus, it is likely that during the transfer of the samples from the FTIR/TPD reactor (where in-situ H_2-pretreatment was performed) to the XPS or XRD setup, samples were exposed to ambient atmospheric conditions which resulted in the re-oxidation. This suggests that the in-situ reduction phenomena and the structural changes observed for the perovskite samples indirectly via FTIR and TPD experiments occur most probably on the surfaces of the materials rather than in the bulk. Furthermore, it is apparent that the reduced surfaces can readily be re-oxidized in a rather reversible fashion under ambient conditions.

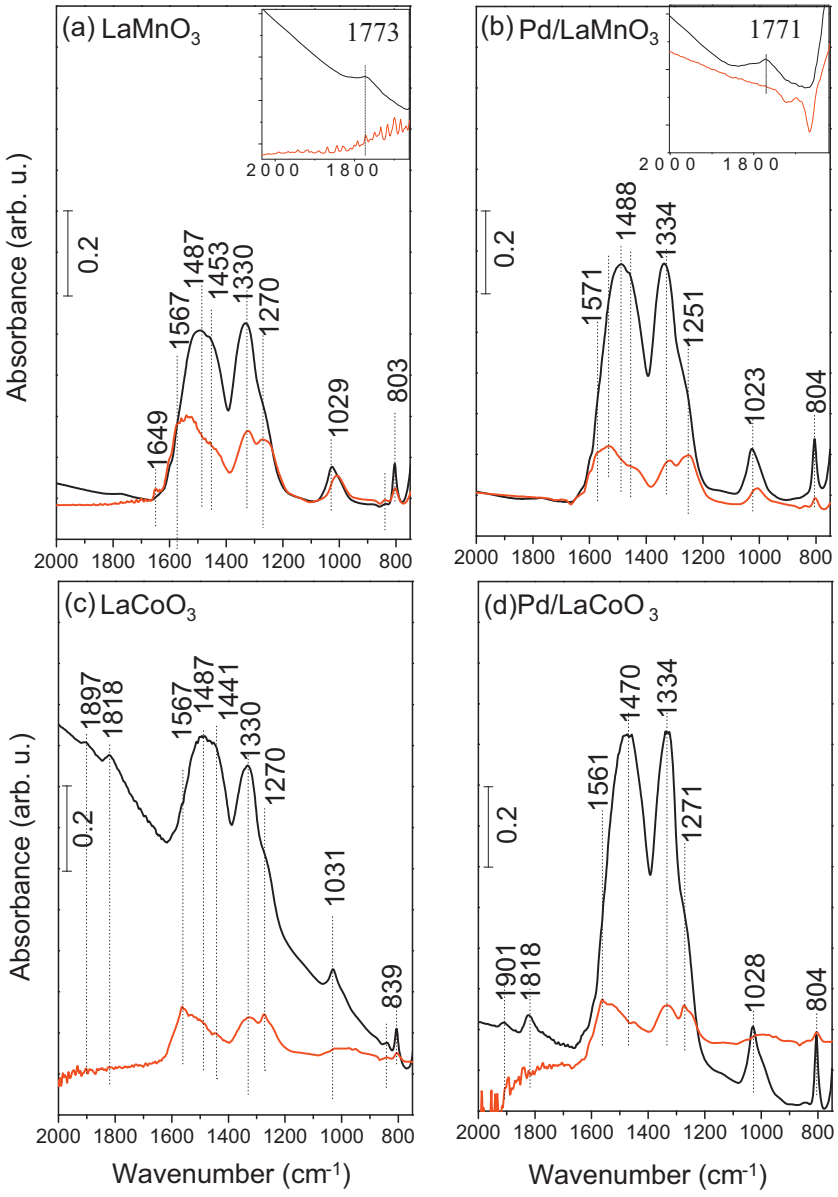

Fig. 10. FTIR spectra corresponding to the NO_2 saturated surfaces of (a) $LaMnO_3$, (b) $Pd/LaMnO_3$, (c) $LaCoO_3$ and (d) $Pd/LaCoO_3$ samples at 323 K. Red spectra in each panel correspond to fresh perovskite surfaces and black spectra correspond to *pre-reduced* (via 5.0 Torr H_2(g) at 623 K for 10 min) perovskite materials. (For interpretation of the references to color in this figure legend, the reader is referred to the web version of this article.)

Complementary TPD experiments were also performed in order to have a clear understanding of the effect of a reducing treatment on NO_x uptake. TPD profiles obtained by saturating the pre-reduced $LaCoO_3$, $Pd/LaCoO_3$, $LaMnO_3$ and $Pd/LaMnO_3$ surfaces with NO_2 at 323 K are illustrated in Fig. 11. Although the TPD profiles corresponding to fresh $LaMnO_3$ and $LaCoO_3$ (Fig. 11a and d) were already presented in Fig. 8a and c, these data are revisited (and plotted using a different scale) in Fig. 11 for the sake of comparison with the pre-reduced samples. TPD profiles in Fig. 11 are in very good agreement with the FTIR data given in Fig. 10 confirming the drastic increase in the NO_x uptake of all of the H_2-pretreated samples. Quantitatively speaking, in comparison to the fresh $LaMnO_3$ sample, integrated total NO_x desorption signal in TPD increases by 46% in the case of pre-reduced $LaMnO_3$ and by 82% in the case of pre-reduced $Pd/LaMnO_3$ (Fig. 9). In a similar fashion, in comparison to the fresh $LaCoO_3$ sample, integrated total NO_x desorption signal in TPD increases by 101% in the case of pre-reduced $LaCoO_3$ and by 196% in the case of pre-reduced $Pd/LaCoO_3$ (Fig. 9). Furthermore, indications of the radical compositional and electronic changes inferred by the FTIR data given in Fig. 10 are also apparent in the TPD profile of the pre-reduced $LaCoO_3$ (Fig. 11b), where the TPD line shape and the desorption maxima undergo a significant alteration. This is in line with the destruction of the perovskite ABO_3 lattice to a certain extent upon H_2(g) pre-treatment and the formation of $Co^0/CoO/La_2O_3$ [17]. Another very important aspect of the pre-reduced $LaCoO_3$ TPD results (Fig. 11b) is the strong low temperature (i.e. 420 K) N_2 and N_2O evolution, indicating the capability of this pre-reduced surface to directly reduce stored-nitrate/nitrite species. It is possible that the reduced Co^0/Co^{2+} species generated upon H_2-pretreatment are responsible for the enhanced direct NO_x reduction. These intense low-temperature desorption signals can also be associated with the desorption/decomposition of weakly bound dinitrosyl species (illustrated in the FTIR results given in Fig. 10) which are formed on the reduced Co^0/Co^{2+} species. However it is worth emphasizing that due to the relatively low desorption temperature of all of the NO_x species, pre-reduced $LaCoO_3$ sample does not seem to possess a significant high-temperature NO_x adsorption capability.

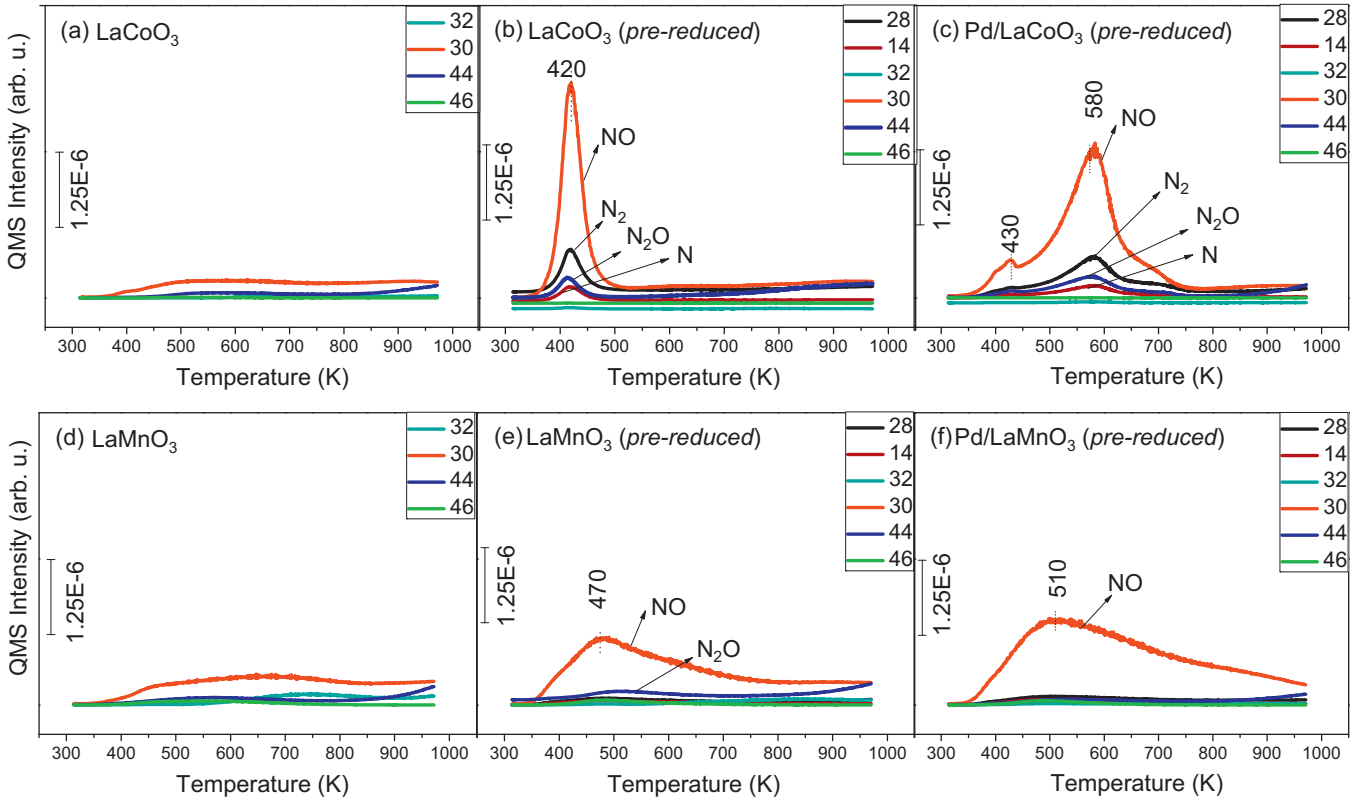

Fig. 11. TPD profiles obtained after NO_2 saturation (via 5 Torr NO_2(g) at 323 K for 10 min) of (a) $LaCoO_3$, (b) *pre-reduced* $LaCoO_3$, (c) *pre-reduced* $Pd/LaCoO_3$, (d) $LaMnO_3$, (e) *pre-reduced* $LaMnO_3$ and (f) *pre-reduced* $Pd/LaMnO_3$ surfaces.

Comparison of the TPD data for the pre-reduced $LaCoO_3$ and pre-reduced $Pd/LaCoO_3$ samples (Fig. 11b and c, respectively) suggest that Pd addition has three major effects on the NO_x uptake behavior of the Co-based perovskite systems. First, Pd addition and H_2-pretreatment (Fig. 11c) further boosts the NO_x uptake of the pre-reduced $LaCoO_3$ (Fig. 11b) by about 52% based on the total NO_x desorption signal in TPD (Fig. 9). Second, through Pd addition and H_2-pretreatment (Fig. 11c), pre-reduced $Pd/LaCoO_3$ system gains both low-temperature (i.e. 430 K) as well as high-temperature (i.e. 580 K) NO_x storage capabilities without compromising its ability toward direct NO_x reduction and N_2/N_2O production. As a matter of fact, comparison of Fig. 11b and c immediately reveals that the amount of N_2/N_2O generated via direct NO_x reduction is significantly enhanced upon Pd addition and pre-reduction. Third, Pd addition tends to preserve the ABO_3 perovskite structure to a certain extent, since the desorption profiles of pre-reduced $Pd/LaCoO_3$ system (Fig. 11c) somewhat resembles the desorption characteristics of fresh $LaCoO_3$ (Fig. 11a) while this is clearly not true for the pre-reduced $LaCoO_3$ (Fig. 11b). It is likely that in the presence of Pd, H_2 can readily be activated and dissociated on the Pd sites [51]. H-species generated this way can either reduce the local PdO species and form metallic Pd [52] or spill over the perovskite to generate oxygen defects. Such oxygen defect sites can function as strong adsorption sites for NO_2(g) species, forming adsorbed nitrosyls and nitrites which boost the overall NO_x uptake. In a similar fashion, metallic Pd sites formed upon H_2-pretreatment (which are well known to be efficient oxidation catalysts) may also assist the oxidation of NO_2 into nitrates and enhance the NO_x adsorption.

A similar analysis can also be performed for the NO_2 TPD profiles of fresh $LaMnO_3$, pre-reduced $LaMnO_3$ and pre-reduced $Pd/LaMnO_3$ (Fig. 11d–f, respectively). Such an analysis brings three main points into attention. First, both pre-reduction and Pd addition processes have a noticeably positive influence on NO_x uptake of Mn-based perovskite systems. Second, pre-reduction process (in the presence or absence of Pd) does not significantly alter the TPD desorption line shapes or shift the desorption maxima, suggesting that the ABO_3 structure is preserved to a greater extent for Mn-based systems. Third, relative amount of direct NO_x reduction and the formation of N_2/N_2O is less pronounced in Mn-based perovskite systems (Fig. 11d–f).

In overall, the significant boost in NO oxidation and improved NO_x adsorption over Pd promoted and H_2 pretreated Co- and Mn-based perovskites are confirmed by both FTIR and TPD experiments. Although these experiments do not reveal a clear evidence for the origin of this behavior, it is plausible that the increase in the NO_x uptake upon H_2-pretreatment can be associated with the reduction-induced morphological changes such as surface reconstructions, which may increase the specific surface area and hence the NO_x adsorption. Alternatively, the increase in the NO_x uptake upon reduction can also be closely related to the electronic and compositional changes occurring on these surfaces such as the partial/total reduction of the B-site cation (particularly in the case of Co), reduction of PdO species into Pd and/or the formation of surface oxygen defects which may act as additional anchoring sites for NO_x species. Considering the fact that many heterogeneous catalytic applications relevant to automotive industry such as NSR/LNT processes consists of a NO_x storage (lean) cycle followed by a reduction (rich) cycle; Mn and Co-based systems can be considered as promising catalytic materials whose NO_x uptake can be boosted/regenerated via onboard cyclic reduction (rich) treatments.

4. Conclusions

In the current work, perovskite-based materials ($LaMnO_3$, $Pd/LaMnO_3$, $LaCoO_3$ and $Pd/LaCoO_3$) were synthesized,

characterized and their NO_x uptake behavior was investigated as a function of the nature of the B-site cation (i.e. Mn vs Co), Pd incorporation and H_2-pretreatment. Some of the major findings of the current study can be summarized as follows:

- $LaMnO_3$ and $Pd/LaMnO_3$ revealed a cubic perovskite crystal structure, whereas $LaCoO_3$ and $Pd/LaCoO_3$ exposed both cubic and rhombohedral phases after synthesis and calcination at 973 K.
- SSA values for $LaMnO_3$ and $Pd/LaMnO_3$ were significantly higher compared to that of $LaCoO_3$ and $Pd/LaCoO_3$ (20.6 and 21.9 m^2/g vs 7.1 and 8.9 m^2/g, respectively). Along these lines, the amount of NO_x adsorption on $LaMnO_3$ was found to be significantly higher than $LaCoO_3$, in line with the higher SSA of $LaMnO_3$.
- Surfaces of all samples were found to be La-enriched either due to the presence of amorphous surface La_2O_3, $La_2(CO_3)_3$, $La(OH)_3$ domains or La-terminated ABO_3 structure.
- Incorporation of PdO/PdO_x nanoparticles with an average diameter of ca. 4 nm did not have a significant effect on the NO_x adsorption behavior over fresh $LaMnO_3$ and $LaCoO_3$.
- Perovskite materials were found to be capable of activating N–O linkages typically at ca. 550 K (even in the absence of an external reducing agent such as H_2) forming N_2 and N_2O as direct NO_x reduction products.
- H_2-pretreatment yielded a drastic improvement in the amount of NO_x adsorption for all samples, particularly for the Co-based systems. Presence of Pd further boosted the interaction between NO_x and the surface of the H_2-pretreated perovskite.
- Increase in the NO_x adsorption of H_2-pretreated $LaCoO_3$ and $Pd/LaCoO_3$ surfaces could be associated with the changes in their oxidation states (i.e. reduction of B-site cation), structural changes (surface reconstruction and SSA increase), reduction of the precious metal oxide (PdO) into metallic species (Pd) and the generation of oxygen defects on the perovskite. Mn-based systems were found to be more resilient toward B-site reduction.
- Pd-addition was found to suppress the B-site reduction and preserved the ABO_3 perovskite structure.

Appendix A. Supplementary data

Supplementary data associated with this article can be found, in the online version, at http://dx.doi.org/10.1016/j.apcatb.2014.01.038.

References

[1] K. Kato, H. Nohira, K. Nakanishi, S. Iguchi, T. Kihara, H. Muraki, Euro Patent Application 0,573,672 A1, 1993.
[2] N. Myioshi, S. Matsumoto, K. Katoh, T. Tanaka, K. Harada, N. Takahashi, K. Yokota, M. Sugiura, K. Kasahara, SAE Technical Papers Series No. 950809, SAE, 1995.
[3] N. Takahashi, H. Shinjoh, T. Iijima, T. Suzuki, K. Yamazaki, K. Yokota, H. Suzuki, N. Miyoshi, S. Matsumoto, T. Tanizawa, T. Tanaka, S. Tateishi, K. Kasahara, Catalysis Today 27 (1996) 63.
[4] S. Rousseau, S. Loridant, P. Delichere, A. Boreave, J. Deloume, P. Vernoux, Applied Catalysis B: Environmental 88 (2009) 438.
[5] N. Li, A. Boreave, J. Deloume, F. Gaillard, Solid State Ionics 179 (2008) 1396.
[6] M.A. Peña, J.L. Fierro, Chemical Reviews 101 (2001) 1981.
[7] J. Zhu, D. Xiao, J. Li, X. Xie, X. Yiang, Y. Wu, Journal of Molecular Catalysis A: Chemical 233 (2005) 29.
[8] Z. Zhao, X. Yang, Y. Wu, Applied Catalysis B: Environmental 8 (1996) 281.
[9] Y. Zhu, D. Wang, F. Yuan, G. Zhang, H. Fu, Applied Catalysis B: Environmental 82 (2008) 255.
[10] H. Iwakuni, Y. Shinmyou, H. Yano, H. Matsumoto, T. Ishihara, Applied Catalysis B: Environmental 74 (2007) 299.
[11] Y. Wu, C. Cordier, E. Berrier, N. Nuns, C. Dujardin, P. Granger, Applied Catalysis B: Environmental 140–141 (2013) 151.
[12] I. Twagirashema, M. Engelmann-Pirez, M. Frere, L. Burylo, L. Gengembre, C. Dujardin, P. Granger, Catalysis Today 119 (2007) 100.
[13] M. Yung, E. Holmgreen, U. Ozkan, Journal of Catalysis 247 (2007) 356.
[14] M. Irfan, J. Goo, S. Kim, Applied Catalysis B: Environmental 78 (2008) 267.
[15] Y. Wen, C. Zhang, H. He, Y. Yu, Y. Teraoka, Catalysis Today 126 (2007) 400.
[16] C. Kim, G. Qi, K. Dahlberg, W. Li, Science (2010) 1624–1627.
[17] I. Twagirashema, M. Frere, L. Gengembre, C. Dujardin, P. Granger, Topics in Catalysis 42–43 (2007) 171.
[18] M. Engelmann-Pirez, P. Granger, L. Leclercq, G. Leclercq, Topics in Catalysis 30–31 (2004) 59.
[19] C. H. Kim, W. Li, K. A. Dahlberg, US Patent 7, 964, 167 B2.
[20] E. Kayhan, S.M. Andonova, G.S. Senturk, C.C. Chusuei, E. Ozensoy, Journal of Physical Chemistry C 114 (2010) 357.
[21] P. Basu, T.H. Ballinger, J.T. Yates Jr., Review of Scientific Instruments 59 (1988) 1321.
[22] Z. Say, E.I. Vovk, V.I. Bukhtiyarov, E. Ozensoy, Applied Catalysis B: Environmental 142–143 (2013) 89.
[23] M. Popa, M. Kakihana, Solid State Ionics 151 (2002) 251.
[24] X. Zhoua, Y. Zhao, X. Cao, Y. Xue, D. Xua, L. Jiang, W. Su, Materials Letters 62 (2008) 470.
[25] E. Granado, N.O. Moreno, A. Garcia, J.A. Sanjurjo, C. Rettori, I. Torriani, Physical Review B: Condensed Matter 58 (1998) 11435.
[26] W. Li, G.V. Gibbs, S.T. Oyama, Journal of American Chemical Society 120 (1998) 9041.
[27] B. Ammundsen, G.R. Burns, M.S. Islam, H. Kanoh, J. Rozière, Journal of Physical Chemistry B 103 (1999) 5175.
[28] J.M. Giraudon, A. Elhachimi, F. Wyrwalski, S. Siffert, A. Aboukais, J.F. Lamonier, G. Leclercq, Applied Catalysis B: Environmental 75 (2007) 157.
[29] L. Xi, Z. Peng, W. Fan, K. Guo, J. Gu, M. Zhao, J. Meng, Materials Chemistry and Physics 46 (1996) 50.
[30] M.N. Iliev, M.V. Abrashev, H.G. Lee, V.N. Popov, Y.Y. Sun, C. Thomsen, R.L. Meng, C.W. Chu, Physical Review B: Condensed Matter 57 (1998) 5.
[31] C.W. Tanga, C.B. Wang, S.H. Chien, Thermochimica Acta 473 (2008) 68.
[32] Y. Wu, X. Ni, A. Beaurain, C. Dujardin, P. Granger, Applied Catalysis B: Environmental 125 (2012) 149.
[33] Z. Chen, C.H. Kim, L.T. Thompson, W.F. Schneider, Surface Science (2013), http://dx.doi.org/10.1016/susc.2013.09.012.
[34] F.E. López-Suárez, M.J. Illán-Gómez, A. Bueno-López, J.A. Anderson, Applied Catalysis B: Environmental 104 (2011) 261.
[35] B. Klingenberg, M.A. Vannice, Applied Catalysis B: Environmental 21 (1999) 19.
[36] A. Martinez-Arias, J. Soria, J.C. Conesa, X.L. Seoane, A. Arcoya, R. Cataluna, Journal of Chemical Society, Faraday Transactions 91 (11) (1995) 1679.
[37] K.I. Hadjiivanov, Catalysis Reviews—Science and Engineering 42 (2000) 71.
[38] F. Prinetto, G. Ghiotti, I. Nova, L. Lietti, E. Tronconi, P. Forzatti, Journal of Physical Chemistry B 105 (2001) 12732.
[39] G. Ghiotti, A. Chiorino, Spectrochimica Acta A49 (1993) 1345.
[40] M.J.D. Low, R.T. Yang, Journal of Catalysis 34 (1974) 3479.
[41] Y. Yokoi, H. Uchida, Catalysis Today 42 (1998) 167.
[42] V.A. Bondzie, P. Kleban, D.J. Dwyer, Surface Science 347 (1996) 319.
[43] M. Crespin, W.K. Hall, Journal of Catalysis 69 (1981) 359.
[44] J.P. Dacquin, C. Dujardin, P. Granger, Journal of Catalysis 253 (2008) 37.
[45] J.P. Dacquin, C. Dujardin, P. Granger, Catalysis Today 137 (2008) 390.
[46] C. Dujardin, I. Twagirashema, P. Granger, Journal of Physical Chemistry 112 (2008) 17183.
[47] T. Montanari, O. Marie, M. Daturi, G. Busca, Applied Catalysis B: Environmental 71 (2007) 216.
[48] K. Hadjiivanov, D. Klissurski, G. Ramis, G. Busca, Applied Catalysis B: Environmental 7 (1996) 251.
[49] K. Hadjiivanov, E. Ivanova, M. Daturi, J. Saussey, J.C. Lavalley, Chemical Physics Letters 370 (2003) 712.
[50] X. Wang, M. Zhou, L. Andrews, Journal of Physical Chemistry A 104 (2000) 7964.
[51] J.A. Rodriguez, D.W. Goodman, Journal of Physical Chemistry 95 (1991) 4196.
[52] M. Blanco-Rey, D.J. Wales, S.J. Jenkins, Journal of Physical Chemistry C 113 (2009) 16757.